IEEE Access
Multidisciplinary | Rapid Review | Open Access Journal

Received April 3, 2019, accepted April 28, 2019, date of publication May 1, 2019, date of current version May 16, 2019.

Digital Object Identifier 10.1109/ACCESS.2019.2914334

Control of a Type-IV Wind Turbine With the Capability of Robust Grid-Synchronization and Inertial Response for Weak Grid Stable Operation

SHUN SANG[1], (Student Member, IEEE), CHEN ZHANG[2], XU CAI[1], MARTA MOLINAS[2], (Member, IEEE), JIANWEN ZHANG[1], (Member, IEEE), AND FANGQUAN RAO[1]

[1]Wind Power Research Center, School of Electronic Information and Electrical Engineering, Shanghai Jiao Tong University, Shanghai 200240, China
[2]Department of Engineering Cybernetics, Norwegian University of Science and Technology, 7491 Trondheim, Norway

Corresponding author: Xu Cai (xucai@sjtu.edu.cn)

This work was supported in part by the National Natural Science Foundation of China under Grant 51677117, and in part by the Power Electronics Science and Education Development Program of Delta Environmental and Educational Foundation under Grant DREM2016005.

ABSTRACT With the increasing penetration of wind power, the effective inertia of the power system reduces. Besides, a series of interactive instability issues including sub-synchronous oscillations and harmonic oscillations were reported due to the weak grid effects. Broadly speaking, those issues are closely related to the PLL and its tuning. Therefore, recent literature make efforts to avoid using the PLL for converter control, e.g., the virtual synchronous generator (VSG) control. However, the VSG control usually employs multiple loops, where a fast switching frequency of the converter is required to decouple each loop's dynamic. This prerequisite is usually not met for wind power converters with high capacity and low switching frequency. To address these issues but also inherit the merits of a VSG on the grid-integration, this paper employs a new concept of PLL-less control and applies it to the Type-IV wind turbine, in which the grid-synchronization is realized by the dynamics of dc capacitor voltage. The virtual capacitor control is designed and added to the machine-side converter to eventually deliver adequate inertia to the grid. To justify the effectiveness of the proposed control, both the soft start-up validation and the thorough analysis of the overall small-signal stability are presented. Several concerns of vital importance regarding the virtual capacitor design and stabilization control are discussed, where the mechanism of stability is revealed through the complex-power coefficient-based analysis. On this basis, a stabilization control method is proposed, which can enlarge the stable range of virtual capacitor coefficient and enhance the inertial response effect. Finally, the performance of the proposed method on the inertial response and the weak grid operation is evaluated by time domain simulations in PSCAD/EMTDC, which is proven effective overall.

INDEX TERMS Wind power generation, weak grid, inertial response, stability analysis, state space model.

I. INTRODUCTION

With the increasing penetration of wind power integrated to the grid [1], in particular with the disperse grid-integration of large wind turbines, the grid can no longer be viewed as stiff for wind power due to the large impedance of transmission systems as well as the lack of inertial support from wind turbines [2]. For a Type-IV wind turbine (i.e. power is processed by a full-scale converter), the grid-side converter (GSC) is generally controlled by the conventional vector control strategy, where the performance of current control can be deteriorated if the grid short circuit ratio (SCR) is low (i.e. the grid impedance seen from wind turbines is large). In this regard, a variety of instability issues has been reported, e.g. the low-frequency oscillations [3], sub-synchronous oscillations [4], [5], high-frequency harmonic oscillations [6]–[8] or more generally the electromechanical oscillations [9]. Moreover, aside from the effects of large grid impedances, lacking inertial support from wind turbines [10] also makes the grid relatively weak from an

The associate editor coordinating the review of this manuscript and approving it for publication was Fabio Massaro.

electromechanical viewpoint [11], i.e. the transient frequency behavior, which may lead to frequency failure if proper countermeasures are not taken [12]. Therefore, there is an urgent need to develop a control strategy of the wind power converter that explicitly addresses these issues in order to achieve good grid-frequency support as well as stable operation.

The problem of wind turbines providing no inertial response is due to the fact that, the phase-locked loop (PLL) in combination with the fast current vector control lacking of frequency support function makes the wind turbine immune to grid frequency changes. Since the rotating wind rotors and generators store a lot of kinetic energy, extracting and using this kinetic energy properly in the control will enable the wind turbine to contribute to the system inertia. To fulfil this, [13] and [14] combined the active power control of the wind turbine with the grid frequency disturbance, through adding a differential signal of the grid frequency to the active power reference. Reference [15] proposed an artificial inertia control strategy, which extracted kinetic energy via modification of the most optimal power curve of the wind turbines dynamically. In [16], the inertia emulation along the entire wind speed section was implemented by the coordination of speed variation and pitch variation control, and the primary frequency regulation was achieved as well. However, large changes of the active power reference during inertia support may lead to overloads and result in the speed stalling of the wind turbine. Hence, impacts of the virtual inertia constant on the wind turbine itself cannot be overlooked. In [17], a secondary fall of frequency in the recovery stage was observed in the Quebec grid of Canada due to the excessive inertia extraction. In general, above-mentioned analysis is based on the modification of current vector controls [13]–[17], which means electrical oscillations primarily caused by interactions between the PLL and current controls under a large grid impedance condition are inevitable [18], [19]. In this regard, substantial analyses have been done recently by means of impedance-based methods [20], [21], where the negative impacts of PLL on small-signal stability of converters are pointed out [22]–[24]. Therefore, considering the negative effects of PLL on vector-controlled converters' stability under weak grid conditions, developing converter controls with the absent of PLL can be promising if at the same time synchronization remains robust.

In this respect, the virtual synchronous generator (VSG) aiming to emulate the electromechanical behavior of a synchronous generator (SG) by converter controls was proposed [25], and hence the grid-synchronization as well as the inertial response can be fulfilled. Zhong and Weiss [26], Nguyen *et al.* [27] proposed the concept of Synchronverter, which emulated the ''swing equation'' of a typical SG to generate the voltage and angle control signals for the converter. In this way, the converter should behave like a SG in terms of the electromechanical dynamics. Another control scheme is the so-called power-synchronization control developed in [28] and [29]. It regulates the converter voltage amplitude and phase angle to dispatch the output reactive and real power, respectively. Analysis results show that the power-synchronization control improves the converter control performance particularly in a weak grid. These preceding control strategies in [25]–[29] can be regarded as the voltage source control, which enables the converter to display the voltage source behavior within the control bandwidth. Compared with the current vector-based controls, the voltage source controls exhibit better stability characteristics. It should be noted that all these above analyses take the output active power as the main control target with the fundamental assumption of a steady dc-link voltage. With respect to the converter whose control objective is the dc-link voltage, the VSG-based methods can be applicable by adding an outer loop, i.e. the dc-link voltage control loop. However, since the dc-link voltage has to be controlled fast, the advantage of an inertial response from the converter is lost. Furthermore, due to the limted switching frequency of wind power converters (typically less than 3 kHz), it is difficult to tune the inner VSG loop for high-speed control. All these concerns are inevitable for a Type-IV wind turbine, making the VSG-based methods inapplicable.

Other than emulating the swing equation of a SG to formulae the VSG control, [30] surveyed the challenges and solutions related to operation and stability control in the power systems with high penetration of renewables. Besides, [30] pointed out that the dc-link voltage of the converter was analogous to the rotational speed of SG in physical mechanism, and this mechanism is further explored and employed in [31] to formulate a new PLL-less control method of three-phase GSC. Reference [31] took the dc-link voltage as the control objective of GSC and adopted the cascaded control structure with outer reactive power loop, middle voltage loop, and inner current loop. An additional frequency droop control loop was also added in the MSC to realize frequency regulation. As mentioned before, the lower switching frequency of high-power wind turbine limits the bandwidth allocation of cascaded control loops and will affect the control performance in [31]. Reference [32] researched the similarities between the dc circuit of converter and the rotor mass of SG, and proposed an oscillator controller for the converter based on the dynamics of dc-link voltage. Besides, droop properties were induced to the controller, which realized frequency regulation and power sharing in a multiple-converter system. Reference [33] developed the model of the virtual synchronous machine (VSM)-based converter, which realized the function of frequency-locked loop through integrating the dc-link voltage. Besides, [33] explored the VSM applied in the scenario of partial generation loss, and pointed out that providing more inertia by the VSM-based converter would cause small-signal instability. But [33] did not analyze the instability mechanism and present the stabilization method.

The above-mentioned analyses lay a great foundation on the new concept of PLL-less control [30]–[33]. This paper extends this idea to the wind power converter system with more focuses on stability assessment, particularly when providing the inertial response under weak grid conditions.

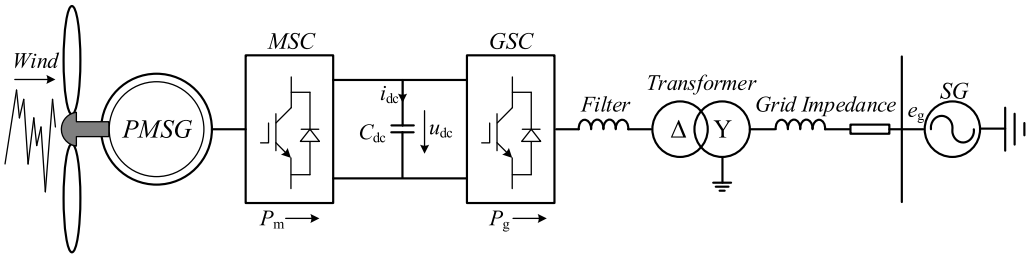

FIGURE 1. Configuration of the wind turbine system with the full-scale converter connected to a weak grid.

Towards this end, this paper proposes a comprehensive control method for the Type-IV wind turbine, including the self-synchronization control (i.e. inertia synchronization control, ISynC) of the GSC, the virtual capacitor control of the MSC, and the stabilization control of the GSC. The start-up process of GSC under such grid-synchronization method is provided and validated, which is crucial from a practical viewpoint. Then, to evaluate the overall stability and have a full picture of the stability trends under various parameters, eigenvalue analysis based on a developed state-space model is conducted. Furthermore, impacts of dominating parameters on the system stability are investigated by the eigenvalue loci. The ''complex power coefficient method'' is adopted to reveal the mechanism of instability from the perspective of damping characteristics. Afterward, this mechanism analysis is utilized for proposing an ancillary stabilization control method, aiming to solve the potential instability issue mentioned in [33]. Finally, the effectiveness of the proposed ISynC on inertial response and weak grid operation, as well as the correctness of small-signal stability analyses, are all verified by simulations in PSCAD/EMTDC.

The remainder of this paper is organized as follows. Section II presents control schematics and operation principles highlighting the properties of the new control proposition. Section III discusses the development of state space model. Section IV presents stability analysis. Section V gives a stabilization control method. Section Vi provides simulations based on PSCAD/EMTDC. Section VII concludes this paper.

II. SYSTEM CONFIGURATION AND CONTROL PRINCIPLES

The investigated system is shown in Fig. 1. It is composed of a permanent magnetic synchronous generator (PMSG), a back-to-back wind power converter, a step-up transformer, as well as a Thevenin equivalent grid with an equivalent impedance which can be obtained from the grid SCR.

A. PRINCIPLE OF THE ISYNC FOR THE GSC

In this section, the ISynC for the GSC will be presented. It adopts the intrinsic dynamics of the converter dc-link capacitor to achieve grid-synchronization. The control principle is introduced as follows.

In Fig. 1, the dynamic equation of the dc-link voltage is given by

$$2H_C\left(u_{dc0}\frac{du_{dc}}{dt}\right) = P_m - P_g \tag{1}$$

where $P_{\rm m}$ is the per-unit output power of the MSC, $P_{\rm g}$ is the per-unit output power of the GSC, $u_{\rm dc}$ is the per-unit dc-link voltage, $u_{\rm dc0}$ is the per-unit value of the steady-state dc-link voltage, and $H_{\rm C}$ is the inertia time constant of the capacitor.

The expression of $H_{\rm C}$ in (1) can be obtained as

$$H_C = \frac{CU_{dcn}^2}{2S_n} \tag{2}$$

where C is the dc-link capacitance, U_{dcn} is the rated dc-link voltage, and S_n is the rated capacity of the wind turbine.

Neglecting the loss of the GSC and the resistive component in the grid impedance, the per-unit output power $P_{\rm g}$ is expressed as

$$P_g = \frac{u_t^* u_{dc} e_g}{x_g}\sin\delta \tag{3}$$

where u_t^* is the per-unit GSC's modulation voltage, e_g is the per-unit grid voltage, $x_{\rm g}$ is the per-unit reactance between the GSC and the SG, i.e. the sum of the transmission line reactance, the transformer leakage reactance, and filter reactance, δ is the leading angle of the GSC output voltage with regard to e_g.

On the other hand, the rotor swing equation of the SG is given by

$$2H_J\left(\omega_m\frac{d\omega_m}{dt}\right) = P_M - P_e \tag{4}$$

where P_M is the per-unit mechanical power of the SG, P_e is the per-unit electromagnetic power of the SG, $\omega_{\rm m}$ is the per-unit rotational speed of the rotor, and H_J is the inertia time constant of the rotor.

The electromagnetic power P_e in (4) can be expressed as

$$P_e = \frac{\psi\omega_m e_g}{x_G}\sin\delta_G \tag{5}$$

where ψ is the per-unit magnetic flux linkage, x_G is the per-unit sum of the transmission line reactance, the transformer leakage reactance, and the SG's synchronous reactance, $\delta_{\rm G}$ is the power angle of the SG.

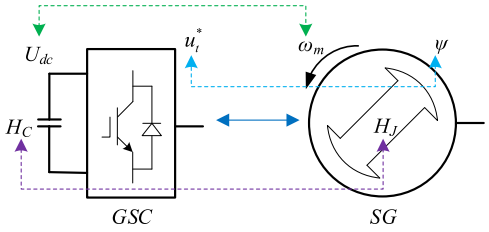

FIGURE 2. Analogy relationship between the GSC and the SG.

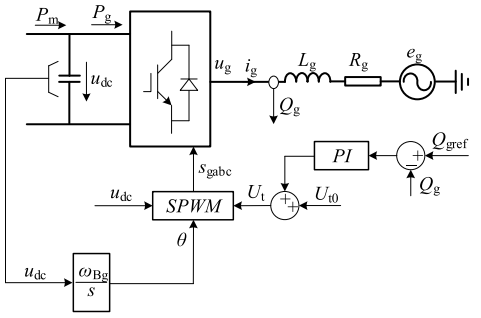

FIGURE 3. Configuration of the proposed ISynC strategy for the GSC.

Comparing (1) with (4), it can be seen that the dc-link voltage u_{dc} has similar dynamic characteristics as the SG's rotational speed ω_m. According to the similarity principle of the dynamical system, the per-unit GSC's modulation voltage u_t^* in (3) is analogous to the magnetic flux linkage ψ in (5). Moreover, the inertia time constant H_C of the capacitor in (1) is analogous to the inertia time constant H_J of the rotor in (4). The relationships between these preceding variables are shown in Fig. 2.

The expression of SG's power angle δ_G with regard to the rotor speed ω_m is obtained by

$$\frac{d\delta_G}{dt} = \omega_{Bg}\left(\omega_m - \omega_g\right) \tag{6}$$

where ω_{Bg} is the base value of grid angular frequency, i.e. 100π rad/s, ω_g is the per-unit grid frequency, i.e. 1.0 p.u. in this paper.

Following the above analogy, to imitate the relationship between δ_G and ω_m, the link of the phase difference δ between the GSC output voltage and grid voltage with regard to the dc-link voltage u_{dc} can be established in the control loop as

$$\frac{d\delta}{dt} = \omega_{Bg}\left(u_{dc} - \omega_g\right). \tag{7}$$

Fig. 3 shows the schematic diagram of the ISynC strategy for the GSC. L_g is the equivalent grid inductance, i.e. the sum of the transmission line inductance, the transformer leakage inductance, and filter inductance. R_g is the equivalent grid resistance. As shown in Fig. 3, according to (7), the per-unit dc-link voltage u_{dc} is input to an integral controller, and the output of this controller is utilized as the phase θ of the GSC's output voltage u_g for pulse width modulation (PWM). The output reactive power Q of GSC can be adjusted by regulating the amplitude U_t of the GSC's modulation voltage. The PWM module generates three-phase switching signals s_{gabc} on the basis of θ, U_t, and u_{dc}.

As it can be seen from Fig. 3, since the control strategy adopts the physical inertia of the dc-link capacitor to serve as an energy buffer for the non-PLL grid synchronization, and omits the "swing equation" of virtual synchronous generator in the control loop, it is named as inertia synchronization control. Furthermore, according to (7), due to the small inertia of the dc-link capacitor, $u_{dc} \approx \omega_g$ is met in the electromechanical time-scale, which means ISynC has a capability of mirroring the ac grid frequency to the dc-link voltage. This remarkable feature can be used for non-communication based inertial response, i, e, the inertial response of a MSC or a sending-end VSC of the high-voltage dc (HVDC) system by measuring the local dc-link voltage.

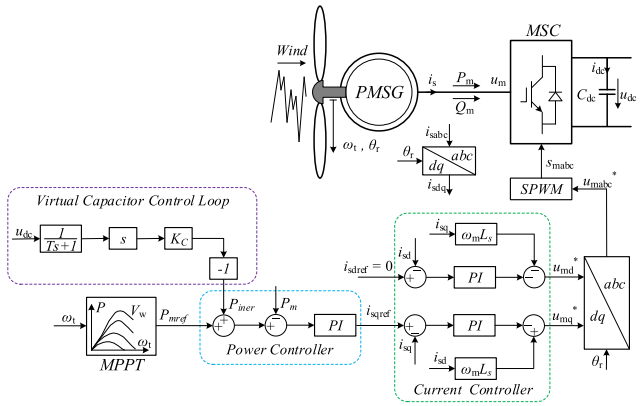

FIGURE 4. Control schematic of the MSC.

B. CONTROL OF THE MSC

The MSC adopts the vector control scheme based on the orientation of rotor flux linkage, where the control structure contains the inner current loop and the outer power loop. Fig. 4 shows the control schematic of the MSC. The position angle θ_r of the rotor flux linkage is measured through the shaft encoder, which provides the phase for the stator current transforming from the stationary frame to the rotated d-q frame. In Fig. 4, the maximum power point tracking (MPPT) control is realized by calculating the active power reference P_{mref} based on the wind turbine speed ω_t. The relationship between P_{mref} and ω_t can be expressed as in (8), where kopt is the optimal power coefficient.

$$P_{mref} = k_{opt}\omega_t^3. \tag{8}$$

In the rotated d-q frame, since the magnetic flux linkage ψ_r of the rotor aligns with the d axis, the output real power of the PMSG is proportional to the q-axis current i_{sq} when the d-axis current i_{sd} of the stator is set to be zero. Therefore, as shown in Fig. 4, the output of the real power controller is set as the q-axis current reference i_{sqref}, and the d-axis current reference i_{sdref} is zero. To eliminate the coupling between the d-axis and q-axis currents, the decoupling elements are added in the current controller. The outputs of this current controller

are transformed from the rotated d-q frame to the stationary frame for PWM.

C. VIRTUAL CAPACITOR CONTROL

As seen from (1), the inertia provided by the ISynC is the physical inertia of the dc-link capacitor, which is small in general. In order to increase the available inertia, the kinetic energy stored in the wind rotor and generator can be utilized. This can be fulfilled by introducing a virtual capacitor control loop to the input of the active power control loop as shown in Fig. 4. The virtual capacitor control strategy detects the change rate of dc-link voltage, and multiplies this change rate by a virtual capacitor coefficient K_C. The result is multiplied by -1 and then added to the active power reference P_{mref}. Since the dc-link voltage contains high-frequency harmonics which will bring in large disturbances through a differentiation element and yield instability, a low-pass filter is added in the virtual capacitor control loop. The principle of virtual capacitor control is shown as below.

In the large time scale of inertial response neglecting the low-pass filter, the output Piner of the virtual capacitor control loop is expressed as

$$P_{iner} = -K_C \frac{du_{dc}}{dt}. \tag{9}$$

Neglecting the response time of control loop, the MSC's output power P_m is given by

$$P_m = P_{mref} - K_C \frac{du_{dc}}{dt}. \tag{10}$$

Substituting (10) into (1), there is

$$2\left(H_C + \frac{K_C}{2u_{dc0}}\right)\left(u_{dc0}\frac{du_{dc}}{dt}\right) = P_{mref} - P_g. \tag{11}$$

According to (11), the equivalent inertia time constant H_{VC} of the capacitor with the virtual capacitor control can be expressed as follows

$$H_{VC} = H_C + \frac{K_C}{2u_{dc0}}. \tag{12}$$

As seen from (12), the total inertia seen from the grid is H_{VC}. By increasing the virtual capacitor coefficient K_C, the equivalent inertia H_{VC} can be enlarged. However, the capability of inertial response is fundamentally determined by the physical limits of the system, i.e. the total kinetic energy stored in the wind rotors including the generator. In addition, increasing the control gain excessively will lead to overloads, the stalling of wind turbines, and has negative effects on the recovery period, e.g. the secondary frequency drop. Therefore, the design of the virtual capacitor coefficient K_C should be within such limits. The upper limit of the equivalent inertia time constant H_{VC} is set as the physical inertia time constant H_{WT} of the wind turbine and PMSG, which can transfer the physical inertia of the wind turbine to the grid. In Table 1 below, H_{WT} is 4, and H_C is approximately 0. It can be obtained from (12) that the upper limit of the virtual capacitor coefficient K_C is 8, which is the K_C value taken for inertia response in Fig. 24 and Fig. 25 below. In fact, due to the attenuation of the low-pass filter in the virtual capacitor control loop, the upper limit value of the K_C can be tuned bigger than 8. This above analysis is based on the ideal response of the MSC control loops. If the control delays are considered, impacts of K_C should be evaluated as presented in the following sections.

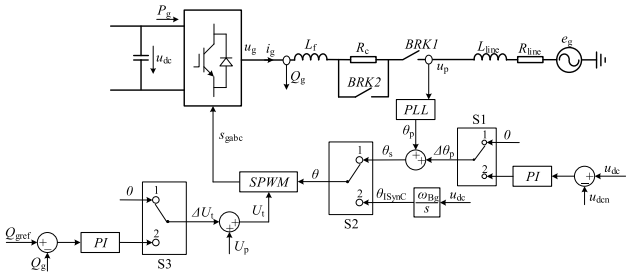

FIGURE 5. Control schematic of the GSC in the start-up process.

D. START UP OF THE GSC

In the start-up process of the ISynC-based wind turbine, the GSC starts before the MSC. Fig. 5 shows the control schematic of the GSC in the start-up process. In Fig. 5, before switching signals s_{gabc} of the GSC's power switching devices are activated, the Switch S1, S2 and S3 are turned to position 1. The PLL is adopted to observe the phase θ_p of the point of common connection (PCC), and the voltage amplitude U_p of the PCC before starting up is utilized as the amplitude of voltage signals for sinusoidal pulse width modulation (SPWM). The start-up process of the GSC is shown as below.

Step 1. The breaker BRK2 is switched off, which means the pre-charging resistor R_c is put in the main circuit and it can limit the charging current of the dc-link capacitor. The breaker BRK1 is switched on, which means the wind turbine is connected to the utility grid. Through the rectification the GSC's diodes, the dc-link capacitor can be charged to the voltage level of the grid's line-line voltage amplitude, which is lower than the rated dc-link voltage. After the voltage of dc-link capacitor reaches the steady-state value, the breaker BRK2 is switched on and the pre-charging resistor R_c is cut out from the main circuit.

Step 2. The switching signals s_{gabc} is activated. Since the phase of GSC's output voltage is close to that of the PCC voltage, the transient current of the GSC in the start-up process is relatively small. Then, to maintain the dc-link voltage at the rated value, the Switch S1 is turned to position 2. The difference between the dc-link voltage u_{dc} and the rated dc-link voltage u_{dc}n, i.e. 1.0 p.u., is put into a proportional integral (PI) controller. The output of PI controller is $\Delta\theta$p, which is added to the output phase θ_p of PLL as the phase θs for SPWM.

Step 3. After the dc-link voltage reaches the rated value, i.e. 1.0 p.u., the Switch S2 is turned to position 2, which means the ISynC is activated in the control loop. It should be noted

that the initial value of the integrator output phase θ_{ISynC} at the switching time is set as the value θ_s in the position 1.

Step 4. After the dc-link voltage reaches the steady-state value under the ISynC, the Switch S3 is turned to position 2, which means the reactive power control is activated. The output of the reactive power controller is added to modulation voltage amplitude U_{p} for SPWM, which can adjust the GSC's output reactive power Q_{g} to the reference value Q_{gref}.

After the GSC starts up, the dc-link voltage is established at the rated value. Then, the MSC starts up as the classical vector-controlled wind turbine. The start-up process of the MSC is not presented in details here.

III. STATE SPACE MODELING OF THE WIND TURBINE SYSTEM

With the ISynC strategy and supplementary artificial capacitor control, the wind turbine imitates the SG so as to engage in power system regulation. Nevertheless, weakly damped oscillations caused by the introduction of virtual capacitor control are prone to arise, especially under weak grid conditions. In this section, the state space model of the wind turbine system is established for stability analysis.

Neglecting the fluctuation of wind turbine speed ω_{t}, the PMSG can be equivalent to an ideal voltage source cascaded with a synchronous inductance L_{s}. In the rotated d-q frame, linearizing the control loop of the MSC in Fig. 4 around its steady-state operation point, the small-signal control diagram of the MSC is shown in Fig. 6. It should be noted that these small-signal variables in Fig. 6 are all transformed into per-unit values.

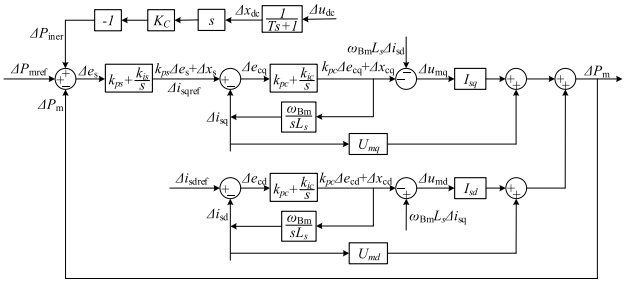

FIGURE 6. Small-signal control diagram of the MSC.

In Fig. 6, the relationship between the output $\Delta_{x_{\mathrm{dc}}}$ and the input Δu_{dc} of the low-pass filter is given by

$$\frac{d\Delta x_{dc}}{dt} = \frac{1}{T}\Delta u_{dc} - \frac{1}{T}\Delta x_{dc} \tag{13}$$

where T is the time constant of the low-pass filter.

The output ΔP_{iner} of the virtual capacitor control loop can be obtained by

$$\Delta P_{iner} = -\frac{K_C}{T}\Delta u_{dc} + \frac{K_C}{T}\Delta x_{dc}. \tag{14}$$

The state variable $\Delta_{x_{\mathrm{s}}}$ is the output of integral regulator in the active power control loop. Likewise, $\Delta_{x_{\mathrm{cd}}}$ and $\Delta_{x_{\mathrm{cq}}}$ are the output of integral regulators in the d-axis and q-axis current control loop respectively. Neglecting the variation of active power reference, i.e. the small-signal active power reference ΔP_{mref} is zero, the output ac voltage of the MSC in the q axis $\Delta_{u_{\mathrm{mq}}}$ is expressed as

$$\begin{aligned}\Delta u_{mq} = {} & k_{ps}k_{pc}\left(\Delta P_m - \Delta P_{iner}\right) - k_{pc}\Delta x_s \\ & - \Delta x_{cq} + k_{pc}\Delta i_{sq} - \omega_{Bm}L_s\Delta i_{sd}\end{aligned} \tag{15}$$

The linearized active power ΔP_{m} of the MSC is shown as

$$\Delta P_m = U_{md}\Delta i_{sd} + U_{mq}\Delta i_{sq} + I_{sd}\Delta u_{md} + I_{sq}\Delta u_{mq} \tag{16}$$

Since the d-axis current of the stator in steady state Isd is zero, substituting (15) into (16), there is

$$\Delta P_m = \frac{1}{k_1}\begin{bmatrix}\left(U_{md} - I_{sq}L_s\right)\Delta i_{sd} + \left(U_{mq} + k_{pc}I_{sq}\right)\Delta i_{sq} \\ -I_{sq}\Delta x_{cq} - k_{pc}I_{sq}\Delta x_s - k_{ps}k_{pc}I_{sq}\Delta P_{iner}\end{bmatrix} \tag{17}$$

where

$$k_1 = 1 - k_{ps}k_{pc}I_{sq}. \tag{18}$$

The q-axis current reference $\Delta i_{\mathrm{sqref}}$, i.e. the output of the active power controller, can be expressed as

$$\Delta i_{sqref} = \Delta x_s - k_{ps}\Delta P_m + k_{ps}\Delta P_{iner}. \tag{19}$$

The state equations about $\Delta_{x_{\mathrm{s}}}$, $\Delta_{x_{\mathrm{cd}}}$, and $\Delta_{x_{\mathrm{cq}}}$ are obtained as follows:

$$\frac{d\Delta x_s}{dt} = -k_{is}\Delta P_m + k_{is}\Delta P_{iner} \tag{20}$$

$$\frac{d\Delta x_{cd}}{dt} = -k_{ic}\Delta i_{sd} \tag{21}$$

$$\frac{d\Delta x_{cq}}{dt} = -k_{ic}\Delta i_{sq} + k_{ic}\Delta i_{sqref}. \tag{22}$$

Considering the compensation effect of decoupling elements in the current controller, the differential equation of d-axis current $\Delta_{i_{\mathrm{sd}}}$ is given as

$$L_s\frac{d\Delta i_{sd}}{dt} = k_{pc}\omega_{Bm}\Delta e_{cd} + \omega_{Bm}\Delta x_{cd}. \tag{23}$$

Simplifying (23), there is

$$\frac{d\Delta i_{sd}}{dt} = -\frac{k_{pc}\omega_{Bm}}{L_s}\Delta i_{sd} + \frac{\omega_{Bm}}{L_s}\Delta x_{cd}. \tag{24}$$

Similarly, the state equation about Δi_{sq} is obtained as

$$\frac{d\Delta i_{sq}}{dt} = -\frac{k_{pc}\omega_{Bm}}{L_s}\Delta i_{sq} + \frac{\omega_{Bm}}{L_s}\Delta x_{cq} + \frac{k_{pc}\omega_{Bm}}{L_s}\Delta i_{sqref}. \tag{25}$$

In the same manner, linearizing the control loop of the GSC in Fig. 3 around its steady-state operation point, Fig. 7 gives the small-signal control diagram of the GSC, where these small-signal variables are all transformed into per-unit values.

The angle for transmission of variables from the stationary frame to the rotated d-q frame is the output phase θ of the integral controller in Fig. 3, which means the GSC's output

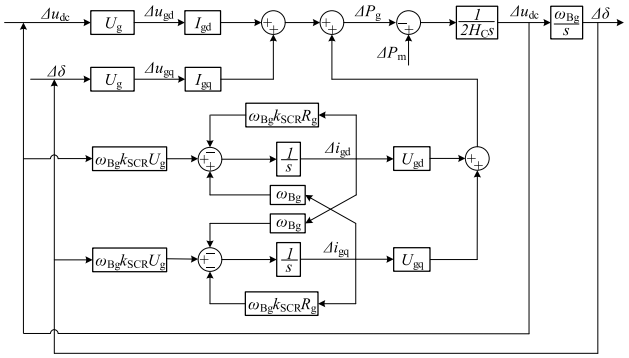

FIGURE 7. Small-signal control diagram of the GSC.

voltage u_{g} is aligned with the d axis. The GSC's output voltage in the d axis and q axis can be expressed as

$$u_{gd} = u^*_{td} u_{dc} \tag{26}$$
$$u_{gq} = u^*_{tq} u_{dc} \tag{27}$$

where u^*_{td}, u^*_{tq} is the per-unit GSC's modulation voltage in the d axis and q axis respectively, u_{dc} is the per-unit dc-link voltage.

Linearizing (26), there is

$$\Delta u_{gd} = u_{dc0}\Delta u^*_{td} + u^*_{td0}\Delta u_{dc} \tag{28}$$

where u_{dc0} is the steady-state per-unit dc-link voltage, i.e. 1.0 p.u., u^*_{td0} is the steady-state per-unit GSC's modulation voltage in the d axis.

Since the oscillation frequencies observed in simulation results of Section VI are 48.2 Hz and 227.3 Hz, which are far bigger than the bandwidth of GSC's reactive power loop, i.e. 5 Hz in this paper, the dynamics of the GSC's reactive power control are ignored, i.e. the amplitude U_t of GSC's modulation voltage is constant without variation. In addition, the modulation voltage u^*_t is aligned with the d axis, thus the followings can be obtained

$$\Delta u^*_{td} = 0 \tag{29}$$
$$u^*_{td0} = U_t = U_g \tag{30}$$

where U_{g} is the per-unit amplitude of GSC's output voltage in steady state.

Substituting (29), (30) into (28), there is

$$\Delta u_{gd} = U_g \Delta u_{dc}. \tag{31}$$

Linearizing (27), there is

$$\Delta u_{gq} = u_{dc0}\Delta u^*_{tq} + u^*_{tq0}\Delta u_{dc} \tag{32}$$

where u^*_{tq0} is the steady-state per-unit GSC's modulation voltage in the q axis. Since the modulation voltage u^*_t is aligned with the d axis, there is

$$u^*_{tq0} = 0. \tag{33}$$

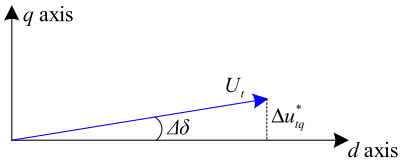

FIGURE 8. Relationship between Δu^*_{tq} and U_t.

The relationship between Δu^*_{tq} and U_t can be shown in Fig. 8. Due to the fact that $\Delta\delta$ is particularly small, Δu^*_{tq} can be expressed as

$$\Delta u^*_{tq} = U_t \sin(\Delta\delta) = U_g \Delta\delta. \tag{34}$$

Substituting (33), (34) into (32), there is

$$\Delta u_{gq} = U_g \Delta\delta. \tag{35}$$

Linearizing the output active power of the GSC, the expression of ΔP_{g} is obtained by

$$\Delta P_g = U_{gd}\Delta i_{gd} + U_{gq}\Delta i_{gq} + I_{gd}\Delta u_{gd} + I_{gq}\Delta u_{gq} \tag{36}$$

where U_{gd}, U_{gq} are the steady-state output voltage of the GSC in the d axis and q axis, I_{gd}, I_{gq} are the steady-state output current of the GSC in the d axis and q axis.

Linearizing the dynamic equation (1) of the dc-link voltage, considering the steady-state value of u_{dc0} is 1, there is

$$2H_C \frac{d\Delta u_{dc}}{dt} = \Delta P_m - \Delta P_g. \tag{37}$$

Since the output ac voltage u_{g} of the GSC is aligned with the d axis, i.e. U_{gq} is zero, substituting (36) into (37), there is

$$\frac{d\Delta u_{dc}}{dt} = -\frac{I_{gd}U_g}{2H_C}\Delta u_{dc} - \frac{I_{gq}U_g}{2H_C}\Delta\delta - \frac{U_g}{2H_C}\Delta i_{gd} + \frac{1}{2H_C}\Delta P_m \tag{38}$$

The state equation about $\Delta\delta$ is obtained by

$$\frac{d\Delta\delta}{dt} = \omega_{Bg}\Delta u_{dc}. \tag{39}$$

The differential equation of the GSC output current Δi_{gd} in the d axis is given by

$$L_g \frac{d\Delta i_{gd}}{dt} = \omega_{Bg}U_g\Delta u_{dc} - \omega_{Bg}R_g\Delta i_{gd} + \omega_{Bg}L_g\Delta i_{gq} \tag{40}$$

where L_g is the per-unit inductance between the GSC and the SG, R_g is the per-unit resistance between the GSC and the SG.

The index k_{SCR} is adopted in this paper to measure the stiffness of a grid [34], which is defined as

$$k_{SCR} = \frac{S_{SC}}{S_N} = \frac{1}{Z_g} \tag{41}$$

where SSC is the short-circuit capacity at the ac side of GSC, SN is the rated capacity of the wind turbine.

Typically, the value of k_{SCR} is above 20 in a stiff grid, and the value of k_{SCR} is below 5 in a weak grid [34]. The value

of k_{SCR} is calculated as the reciprocal of the per-unit grid inductance L_g. The state equation about Δi_{gd} is expressed as

$$\frac{d\Delta i_{gd}}{dt} = k_{SCR}\omega_{Bg}U_g\Delta u_{dc} - k_{SCR}\omega_{Bg}R_g\Delta i_{gd} + \omega_{Bg}\Delta i_{gq}. \tag{42}$$

Similarly, the state equation about the GSC output current Δi_{gq} in the q axis is obtained as

$$\frac{d\Delta i_{gq}}{dt} = k_{SCR}\omega_{Bg}U_g\Delta\delta - k_{SCR}\omega_{Bg}R_g\Delta i_{gq} - \omega_{Bg}\Delta i_{gd}. \tag{43}$$

To establish the state space equation of the ISynC-based wind turbine system, the state vector taken in this paper is

$$\Delta x = [\Delta u_{dc}\ \Delta\delta\ \Delta i_{sd}\ \Delta i_{sq}\ \Delta x_{cd}\ \Delta x_{cq}\ \Delta x_s\ \Delta x_{dc}\ \Delta i_{gd}\ \Delta i_{gq}]^T. \tag{44}$$

Based on (13), (20), (21), (22), (24), (25), (38), (39), (42), and (43), the 10-order eigen equation of the ISynC-based wind turbine system is obtained by

$$\frac{d\Delta x}{dt} = A\Delta x + B\begin{bmatrix}\Delta P_m\\ \Delta i_{sqref}\\ \Delta P_{iner}\end{bmatrix}. \tag{45}$$

Based on (14), (17), and (19), the following can be obtained:

$$\begin{bmatrix}\Delta P_m\\ \Delta i_{sqref}\\ \Delta P_{iner}\end{bmatrix} = C\Delta x. \tag{46}$$

Substituting (46) into (45), there is:

$$\frac{d\Delta x}{dt} = (A + BC)\,\Delta x. \tag{47}$$

According to (47), the 10-order eigen matrix H of the wind turbine system is expressed as

$$H = A + BC. \tag{48}$$

The expression of A, B, and C can be found in (A-1), (A-2), (A-3) of the Appendix.

IV. STABILITY ANALYSIS AND IMPACTS OF CONTROL PARAMETERS

The system configuration and small-signal control diagram of the ISynC-based wind turbine are given in preceding sections, and the state space equation is established. This section will draw the loci of system eigenvalues and analyze impacts of dominating parameters on the system stability under weak grid conditions. Taking a PMSG-based wind turbine system rated at 2 MW as an example, Table 1 presents relevant electrical parameters.

To decouple the response time of the inner current loop and outer power loop, the MSC control parameters are tuned according to the typical controller design method where the current loop bandwidth is 1/10 the switching frequency of MSC, i.e. 200Hz, and the bandwidth of power loop is 10 Hz.

TABLE 1. Electrical parameters of the wind turbine system.

Symbol	Description	Value
S_B	Base power value	2 MW
U_B	Base value of ac phase voltage	0.563 kV
U_{dcB}	Base value of dc-link voltage	1.1 kV
ω_{Bm}	Base value of stator angular frequency	84.6 rad/s
ω_{Bg}	Base value of grid angular frequency	314 rad/s
f_N	Rated frequency of PMSG	13.47 Hz
P	Pole pairs of PMSG	42
ψ_r	magnetic flux linkage of rotor	0.896 p.u.
L_s	synchronous inductance of PMSG	0.5495 p.u.
R_s	Stator resistance of PMSG	0.00387 p.u.
H_{WT}	Inertia constant of wind turbine and PMSG	4 s
H_C	Inertia time constant of dc-link capacitor	3.025 ms
C	Capacitance of dc-link capacitor	10 mF
u_{dc0}	steady-state dc-link voltage	1.0 p.u.
e_g	Equivalent grid phase voltage	1.0 p.u.
f_s	Switching frequency	2 kHz

TABLE 2. Control parameters of the wind turbine system.

Symbol	Description	Value
T	Filter time constant	0.1 s
k_{pc}	Proportional gain of MSC current controller	2.6
k_{ic}	Integral gain of MSC current controller	520
k_{ps}	Proportional gain of MSC power controller	0.05
k_{is}	Integral gain of MSC power controller	10

Table 2 presents relevant control parameters of the wind turbine system.

The eigenvalues of the ISynC-based wind turbine system can be obtained through solving the following equation

$$\det(\lambda I - H) = 0 \tag{49}$$

where I represents the 10×10 identity matrix.

A. IMPACTS OF THE GRID SCR

Based on the electrical and control parameters in Table 1 and 2, Fig. 9 shows the loci of system eigenvalues as a function of SCR under no virtual capacitor control, where T is 0.1 s, and K_C is 0. In Fig. 9, with the decrease of k_{SCR} from 10 to 1, No. 1-4, 9, and 10 poles remain unchanged, and No. 5 and 6 poles shift toward the real axis, which increase relevant damping ratios. No. 7 and 8 poles shift toward the imaginary axis and return. In general, all poles locate in the left half plane, and the ISynC-based wind turbine system still has desired stability margin even in an extremely weak grid with k_{SCR} of 1. Nevertheless, no virtual capacitor control

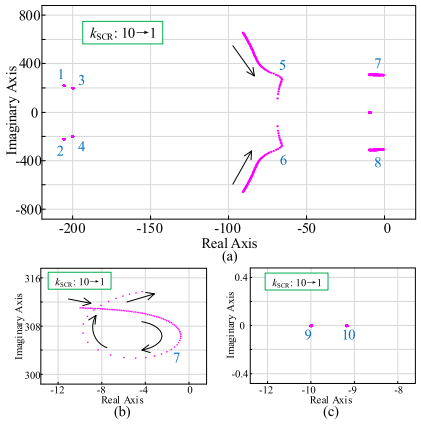

FIGURE 9. Loci of system eigenvalues as a function of SCR with no virtual capacitor control. (a) Overall view. (b) Partial enlarged view I. (c) Partial enlarged view II.

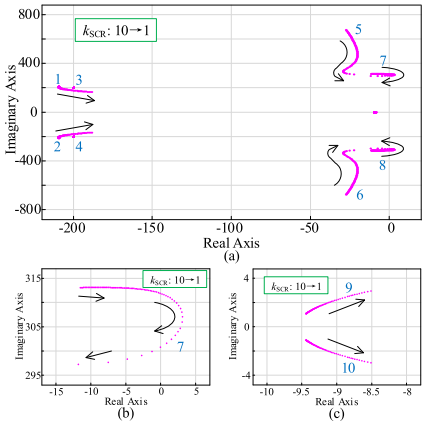

FIGURE 10. Loci of system eigenvalues as a function of SCR with virtual capacitor control. (a) Overall view. (b) Partial enlarged view I. (c) Partial enlarged view II.

means the wind turbine cannot provide inertial response to the grid.

Fig. 10 shows the loci of system eigenvalues as a function of SCR under virtual capacitor control, where T is 0.1 s, and K_C is 0.5. In Fig. 10, with the decrease of k_{SCR} from 10 to 1, No. 3 and 4 poles remain unchanged, and No. 1 and 2 poles shift toward the right but still have enough damping ratios. No. 5 and 6 poles shift toward the real axis, which increase relevant damping ratios. No. 9 and 10 poles shift toward the imaginary axis, which decrease the damping ratios. No. 7 and 8 poles shift toward the right and return, but significant parts of the loci still locate in the right half plane, which means small-signal instability occurs in the wind turbine system. The analysis results based on eigenvalue loci in Fig. 10 indicate that the ISynC-based wind turbine is prone to operate unstably when providing inertial response.

B. IMPACTS OF THE VIRTUAL CAPACITOR COEFFICIENT

To investigate the influence of virtual capacitor control on the stability of wind turbine system, Fig. 11 shows the loci of

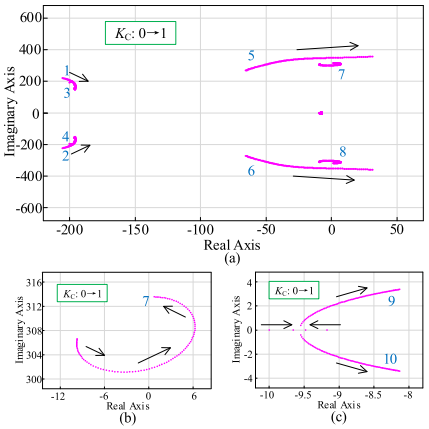

FIGURE 11. Loci of system eigenvalues as a function of virtual capacitor coefficient K_C. (a) Overall view. (b) Partial enlarged view I. (c) Partial enlarged view II.

system eigenvalues as a function of virtual capacitor coefficient K_C, where T is 0.1 s, and k_{SCR} is 2. In Fig. 11, with the increase of K_C from 0 to 1, No. 1-4 poles have enough damping ratios. No. 9 and 10 poles shift away from the real axis and move toward the imaginary axis, which decrease relevant damping ratios. It should be noted that No. 5, 6, 7 and 8 poles move across the imaginary axis to the right half plane, which decrease the damping ratios to negative values and yield instability. Therefore, the virtual capacitor coefficient K_C is not supposed to be too large so that the ISynC-based wind turbine system can operate stably under weak grid conditions.

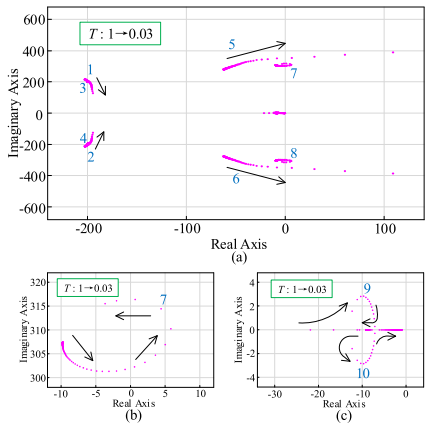

FIGURE 12. Loci of system eigenvalues as a function of filter time constant T with virtual capacitor control. (a) Overall view. (b) Partial enlarged view I. (c) Partial enlarged view II.

C. IMPACTS OF THE FILTER TIME CONSTANT

Fig. 12 shows the loci of system eigenvalues as a function of filter time constant T under virtual capacitor control, where K_C is 0.5, and k_{SCR} is 2. In Fig. 12, with the decrease of T from 1 to 0.03, No. 1-4 poles have enough damping ratios. No. 9 and 10 poles shift toward the imaginary axis but still

locate in the left half plane. Note that No. 5, 6, 7 and 8 poles move across the imaginary axis to the right half plane, which trigger small-signal instability of the wind turbine system. It can be seen from Fig. 12 that increasing the filter time constant will enlarge the system stability margin, but the equivalent gain of the virtual capacitor control decreases, which reduces the extracted inertia from the wind turbine to the grid.

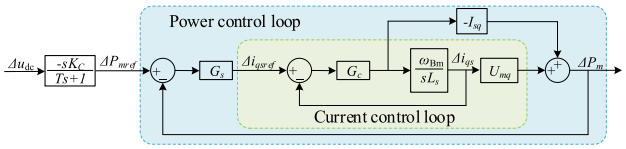

FIGURE 13. Transfer function block diagram from Δu_{dc} to ΔP_m.

D. MECHANISM ANALYSIS OF INSTABILITY

The mechanism analysis is presented in this part by utilizing the "complex power coefficient method" [6] to explain the causes of instability and direct the design of stabilization control method. Simplifying the small-signal control diagram of the MSC in Fig. 6, the transfer function block diagram from Δu_{dc} to ΔP_m is obtained as shown in Fig. 13, where Gs and Gc represent the controller transfer function of the power loop and current loop respectively. According to Fig. 13, the close-loop transfer function of the power control loop can be obtained as

$$\phi_s = \frac{G_s\left(G_C\omega_{Bm}U_{mq} - sG_CL_sI_{sq}\right)}{G_s\left(G_C\omega_{Bm}U_{mq} - sG_CL_sI_{sq}\right) + sL_s + G_C\omega_{Bm}}. \quad (50)$$

Substituting the parameters in Table 1 and 2 into (50), the frequency characteristic of Φs is shown in Fig. 14. It can be seen from Fig. 14 that the phase φs of Φs is less than −90 degrees when the frequency is bigger than 10 Hz. The oscillation frequencies observed in simulation results of Section VI are 48.2 Hz and 227.3 Hz, which corresponds to the phase φs in Fig. 14 between −90 degrees and −180 degrees.

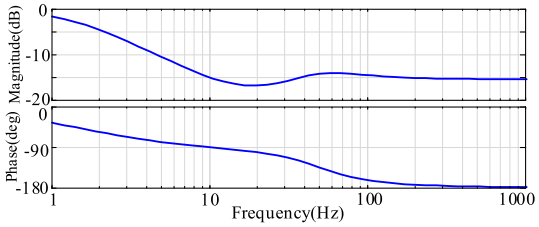

FIGURE 14. Frequency characteristic of Φ s.

According to Fig. 13, the transfer function of ΔP_m about Δu_{dc} can be obtained as

$$\Delta P_m = \frac{-sK_C}{Ts+1}\phi_s\Delta u_{dc}. \quad (51)$$

Substituting (39) into (51), the relationship between $-\Delta P_m$ and $\Delta\delta$ is shown as

$$-\Delta P_m = \frac{K_C}{\omega_{Bg}}\frac{s}{Ts+1}\phi_s s\Delta\delta. \quad (52)$$

Substituting (39) into (37), the relationship between $\Delta\delta$, ΔP_g and $-\Delta P_m$ is shown as

$$\frac{2H_C}{\omega_{Bg}}s^2\Delta\delta + \Delta P_g - \Delta P_m = 0. \quad (53)$$

Since the amplitude of GSC's modulation voltage is constant and k_{SCR} is the reciprocal of the per-unit grid reactance x_g, linearizing the GSC's output active power P_g in (3), there is

$$\begin{aligned}\Delta P_g &= k_{SCR}u^*_{t0}u_{dc0}e_g\cos\delta\Delta\delta + \frac{k_{SCR}u^*_{t0}e_g\sin\delta}{\omega_{Bg}}s\Delta\delta \\ &= K_g\Delta\delta + D_g s\Delta\delta \end{aligned} \quad (54)$$

where K_g is > 0, D_g is > 0. Therefore, $K_g\Delta\delta$ is in phase with $\Delta\delta$, and $D_g s\Delta\delta$ is in phase with $s\Delta\delta$. In this paper, K_g is called the grid-side synchronous power coefficient, and D_g is called the grid-side damping power coefficient.

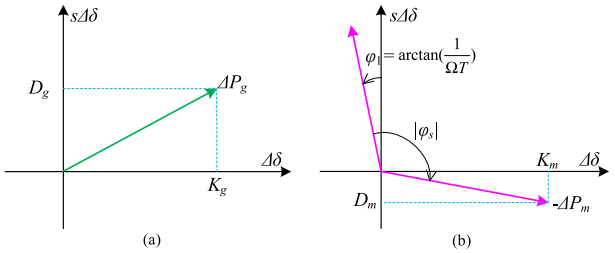

FIGURE 15. Vector diagram of ΔP_g and $-\Delta P_m$. (a) ΔP_g. (b) $-\Delta P_m$.

According to (54) and (52), a vector diagram of ΔP_g and $-\Delta P_m$ on the complex plane with $\Delta\delta$ as the horizontal axis and $s\Delta\delta$ as the vertical axis is shown in Fig. 15. It should be noted that the vectors are obtained at a certain frequency. The complex power ΔP_g of GSC in Fig. 15(a) is decomposed into the grid-side synchronous power and damping power. It can be seen from Fig. 15(a) that the vector ΔP_g is in the 1th quadrant, and D_g is > 0, which corresponds to the positive damping.

In Fig. 15(b), φ_1 is the phase of $\frac{K_C}{\omega_{Bg}}\frac{s}{Ts+1}$, whose value is

$$\varphi_1 = \arctan(\frac{1}{\Omega T}) \quad (55)$$

where Ω is the oscillating angular frequency.

For the oscillation in Section VI with angular frequency of 302.9 rad/s, the value of φ_1 is 1.9 degrees with T of 0.1 s. With the increase of oscillating frequency, the value of φ_1 decreases, thus φ_1 is relatively small and can be ignored. Since φs is between −90 degrees and −180 degrees, the vector $-\Delta P_m$ is in the 4th quadrant, whose amplitude is

$$|-\Delta P_m| = \frac{K_C\Omega}{\omega_{Bg}\sqrt{1+\Omega^2T^2}}|\phi_s|. \quad (56)$$

Similarly, the complex power $-\Delta P_{\mathrm{m}}$ in Fig. 15(b) is decomposed into the machine-side synchronous power and damping power, i.e.

$$-\Delta P_m = K_m \Delta\delta + D_m s\Delta\delta \tag{57}$$

where K_{m} is called the machine-side synchronous power coefficient, D_{m} is called the machine-side damping power coefficient in this paper. Since the vector $-\Delta P_{\mathrm{m}}$ is in the 4th quadrant, K_{m} is > 0, and D_{m} is < 0, which corresponds to the negative damping and leads to instability.

Substituting (54) and (57) into (53), the system characteristic equation can be obtained as

$$\frac{2H_C}{\omega_{Bg}} s^2\Delta\delta + \left(D_g + D_m\right) s\Delta\delta + \left(K_g + K_m\right)\Delta\delta = 0. \tag{58}$$

In (58), when $D_{\mathrm{g}}+D_{\mathrm{m}}$ is > 0, the damping is positive and the system is table. When $D_{\mathrm{g}}+D_{\mathrm{m}}$ is < 0, the damping is negative, which means the system oscillates and diverges. It can be seen from (55) and (56) that the phase of $-\Delta P_{\mathrm{m}}$ is independent of virtual capacitor coefficient K_{C}, and the amplitude of $-\Delta P_{\mathrm{m}}$ is proportional to K_{C}. When K_{C} increases, the corresponding K_{m} increases, and D_{m} decreases. When K_{C} increases to make $D_{\mathrm{g}}+D_{\mathrm{m}} < 0$, oscillation occurs and the system is unstable, which is consistent with the analysis result in Fig. 11 and simulation results in Fig.22 and Fig.23. In addition, decreasing the short-circuit ratio k_{SCR} and filter time constant T will reduce D_{g} and D_{m} respectively, which leads to instability.

V. STABILIZATION CONTROL METHOD

The mechanism explanation in the previous section can help the design of stabilization control method. The design idea of stabilization control method is: If the connection between the GSC's modulation voltage u_t^* and the dc-link voltage u_{dc} is established, the u_t^* cannot be considered constant when linearizing P_{g}, and then the grid-side damping power coefficient can be changed.

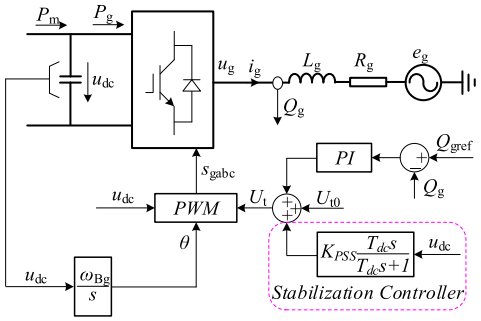

FIGURE 16. Control diagram of the ISynC-based GSC with the stabilization control method.

Fig. 16 shows the control diagram of the ISynC-based GSC with the stabilization control method. In Fig. 16, the stabilization controller processes this input signal via an amplifier gain and a high-pass filter, and the output is added to the modulation voltage amplitude. The high-pass filter allows the dynamic signal to pass smoothly, therefore this stabilization controller only works in the dynamic process.

The auxiliary stabilization control in Fig. 16 builds connection between the dc-link voltage u_{dc} and the GSC's modulation voltage u_t^*. Re-linearizing the GSC's output active power in (3), there is

$$\begin{aligned}\Delta P_g &= K_g\Delta\delta + D_g s\Delta\delta + k_{SCR}u_{dc0}e_g\sin\delta\Delta u_t^* \\ &= K_g\Delta\delta + \left(D_g + D_{PSS}\right)s\Delta\delta\end{aligned} \tag{59}$$

where

$$D_{PSS} = \frac{K_{PSS}k_{SCR}u_{dc0}e_g\sin\delta}{\omega_{Bg}}. \tag{60}$$

It can be seen from (59) that the introduction of feedback control from u_{dc} to the GSC's modulation voltage u_t^* can increase the grid-side damping power coefficient, which helps to improve the system stability.

As we all know, the power system stabilizer (PSS) measures the angular speed of the SG and processes this signal through an amplifier and a high-pass filter. Finally, the output of the PSS is taken as a supplementary signal for excitation. Since the dc-link voltage u_{dc} and modulation voltage u_t^* of the ISynC-based GSC are analogous to the angular speed ω_{m} and magnetic flux linkage ψ of the SG, this stabilization control method proposed in this paper has the stabilization principle as the PSS.

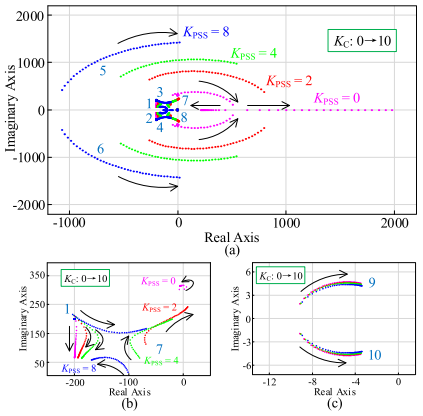

FIGURE 17. Loci of system eigenvalues as a function of virtual capacitor coefficient K_{C} with different amplifier gains. (a) Overall view. (b) Partial enlarged view I. (c) Partial enlarged view II.

Furthermore, considering the auxiliary stabilization controller, the eigen equation of the ISynC-based wind turbine system is established again. Substituting the eigen matrix into (49) and solving the equation, Fig. 17 shows the loci of system eigenvalues as a function of virtual capacitor coefficient K_{C} with different amplifier gains, where T is 0.1 s, and k_{SCR} is 2. In Fig. 17, with the increase of amplifier gain K_{PSS}, the loci of No. 5-8 poles shift toward the left, which increase relevant damping ratios and stability margins. Especially, when K_{PSS} is 8, almost all the loci of system eigenvalues are located in the left half plane with K_{C} from 0 to 10. E.g. in Table 4 of the following section, the system becomes

unstable with the K_C value of 9.87. It can be seen from Fig. 17, with the stabilization control method, increasing the amplifier gain K_{PSS} will improve the stability of the ISynC-based wind turbine system. The analysis results based on eigenvalue loci in Fig. 17 demonstrate the feasibility of the proposed stabilization control method.

VI. SIMULATION VERIFICATION

To verify the effectiveness of the proposed ISynC and stabilization control strategy, time-domain simulations based on PSCAD/EMTDC are conducted in this section. Electrical and control parameters of the test system can be found in Table 1 and Table 2.

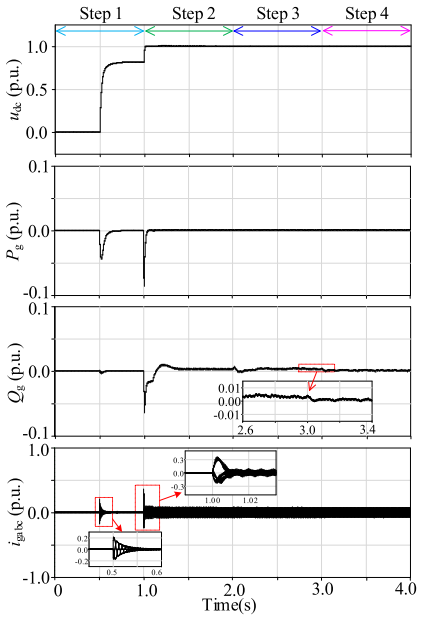

FIGURE 18. Simulation results of the GSC in the start-up process.

A. START UP OF THE GSC

Fig. 18 shows the simulation results of the GSC in the start-up process. In Fig. 18, the breaker BRK1 is switched on at 0.5 s, and the dc-link capacitor is charged through the rectification of the GSC's diodes. At 0.7 s, the breaker BRK2 is switched on, which means the pre-charging resistor Rc is cut out from the main circuit. At 1.0 s, the switching signals s_{gabc} are activated. Then the Switch S1 is turned to position 2, and the dc-link voltage is adjusted to the rated value. At 2.0 s, the Switch S2 is turned to position 2, and the ISynC is activated in the control loop. It can be seen from Fig. 18 the dc-link voltage u_{dc} in the transient process is smooth without distortion. At 3.0 s, the Switch S3 is turned to position 2. The reactive power control is activated, and the GSC's output reactive power Q_g is adjusted to the reference, i.e. 0. As shown in Fig. 18, the transient current of the GSC in the start-up process doesn't exceed the rated value.

B. PERFORMANCE OF DYNAMIC RESPONSES

Fig. 19 shows the simulation results of the ISynC-based wind turbine system with no virtual capacitor control when the grid

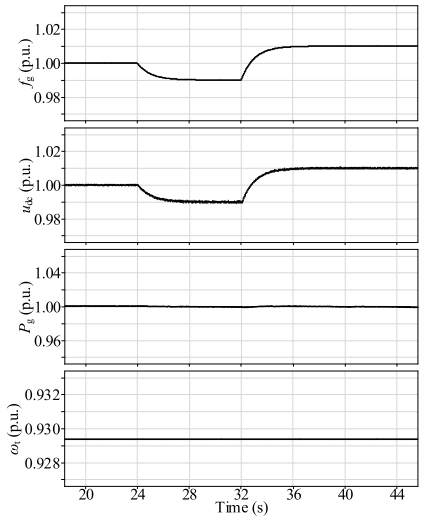

FIGURE 19. Responses of the ISynC-based wind turbine system with no virtual capacitor control when the grid frequency changes.

frequency changes, where K_C is 0, k_{SCR} is 1, and the wind speed is 11 m/s. In Fig. 19, when f_g drops from 1.00 p.u. to 0.99 p.u. at 24 s and rises from 0.99 p.u. to 1.01 p.u. at 32 s, u_{dc} responds accordingly. The change rate of dc-link voltage is similar to that of grid frequency, which validates the analogous relationship between the dc-link voltage and the SG's rotational speed as shown in Fig. 2. During the whole process of grid frequency fluctuating, the output power of the GSC and the wind turbine speed remain almost unchanged, demonstrating the physical inertia of the dc-link capacitor can hardly provide inertial response. Furthermore, the wind turbine system is capable of operating stably even under extremely weak grid conditions with k_{SCR} of 1, which verifies the correctness of theoretical analysis in Fig. 9.

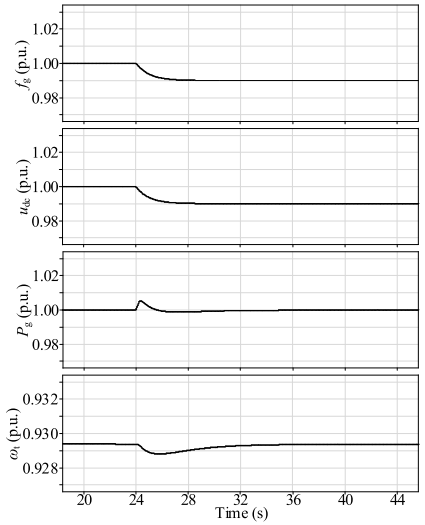

FIGURE 20. Responses of the ISynC-based wind turbine system with virtual capacitor control when the grid frequency drops.

Fig. 20 shows the simulation results of the ISynC-based wind turbine system with virtual capacitor control when the grid frequency drops, where K_C is 0.33, k_{SCR} is 2, and

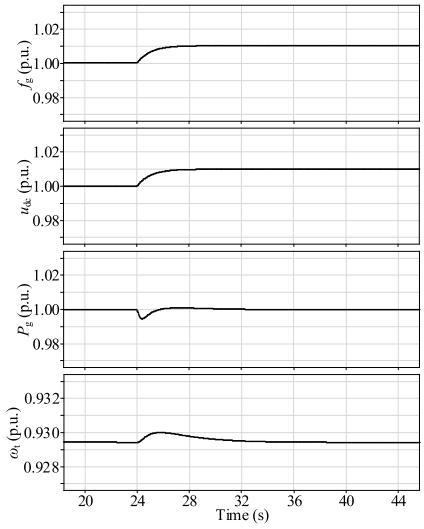

FIGURE 21. Responses of the ISynC-based wind turbine system with virtual capacitor control when the grid frequency rises.

the wind speed is 11 m/s. In Fig. 20, when f_g drops from 1.00 p.u. to 0.99 p.u. at 24 s, u_{dc} drops from 1.00 p.u. to 0.99 p.u. accordingly. Meanwhile, the output power of the GSC increases less than 0.01 p.u., and recovers later. The wind turbine speed decreases approximately 0.001 p.u. and recovers later.

Fig. 21 shows the simulation results of the ISynC-based wind turbine system with virtual capacitor control when the grid frequency rises, where K_C is 0.33, k_{SCR} is 2, and the wind speed is 11 m/s. In Fig. 21, when f_g rises from 1.00 p.u. to 1.01 p.u. at 24 s, u_{dc} rises from 1.00 p.u. to 1.01 p.u. accordingly. Meanwhile, the output power of the GSC decreases less than 0.01 p.u., and recovers later. The wind turbine speed increases approximately 0.001 p.u. and recovers later.

It can be seen from Fig. 20 and Fig. 21 that the ISynC-based wind turbine with virtual capacitor control can provide inertial response when the grid frequency fluctuates, and the response process is entirely autonomous. Meanwhile, the wind turbine system is capable of operating stably under weak grid conditions. The active power absorbed and released by the wind turbine during inertial response is small, which brings fewer benefits to the transient frequency stability of power system.

C. STABILITY COMPARISON

Increasing the virtual capacitor coefficient K_C will enhance the inertial response effect, but it decreases the small-signal stability of the wind turbine system at the same time. Table 3 presents the system eigenvalues with virtual capacitor control, where K_C is 0.45, k_{SCR} is 2. In Table 3, the real parts of No. 1-6 and No. 9-10 poles are all negative, which corresponds to stability. Note that the real parts of No. 7 and 8 poles are positive, which means instability occurs in the wind turbine system and the oscillation frequency is the imaginary part of these two poles, i.e. 302.29 rad/s. Fig. 22 shows simulation results of the ISynC-based wind turbine system

TABLE 3. System eigenvalues with virtual capacitor control.

Poles	Eigenvalues	Stability
No. 1, 2	-196.44 ± j177.29	Stable
No. 3, 4	-200 ± j200	Stable
No. 5, 6	-33.301 ± j335.26	Stable
No. 7, 8	0.39995 ± j302.29	Unstable
No. 9, 10	-8.8705 ± j2.4701	Stable

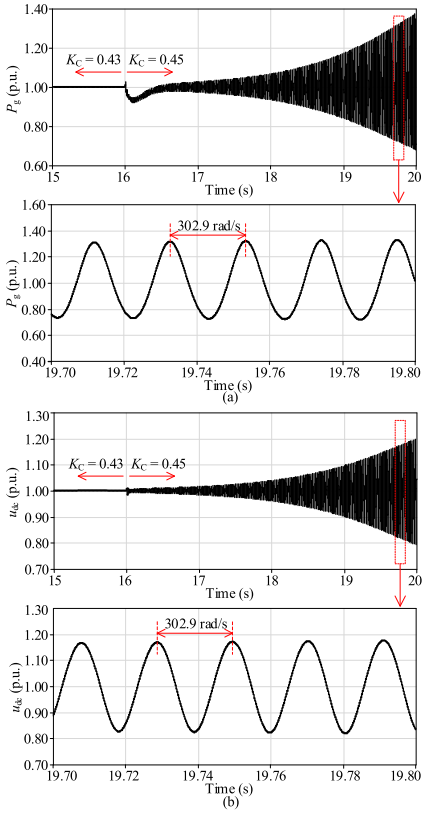

FIGURE 22. Simulation results of the ISynC-based wind turbine system with virtual capacitor control when K_C increases from 0.43 to 0.45. (a) Output power of the GSC. (b) Dc-link voltage.

with virtual capacitor control when K_C increases from 0.43 to 0.45, where k_{SCR} is 2. In Fig. 22, when K_C increases at 16 s, the output power of the GSC and the dc-link voltage begin to oscillate and become unstable. The oscillation frequency in Fig. 22 is 302.9 rad/s, which resembles the analytical oscillation frequency in Table 3, demonstrating the effectiveness of eigenvalue analysis in Fig. 11.

The proposed stabilization control method can expand the stable range of K_C. Table 4 presents the system eigenvalues with virtual capacitor control and stabilization control, where K_C is 9.87, k_{SCR} is 2, and K_{PSS} is 8. In Table 3, the real parts of No. 1-4 and No. 7-10 poles are all negative, which corresponds to stability. It should be noted that the real parts of No. 5 and 6 poles are positive, which means instability occurs in the wind turbine system and the oscillation frequency is the imaginary part of these two poles, i.e. 1424.2 rad/s.

TABLE 4. System eigenvalues with virtual capacitor control and stabilization control.

Poles	Eigenvalues	Stability
No. 1, 2	-69.134 ± j166.23	Stable
No. 3, 4	-200 ± j200	Stable
No. 5, 6	1.0507 ± j1424.2	Unstable
No. 7, 8	-168.47 ± j59.051	Stable
No. 9, 10	-3.4056 ± j4.2183	Stable

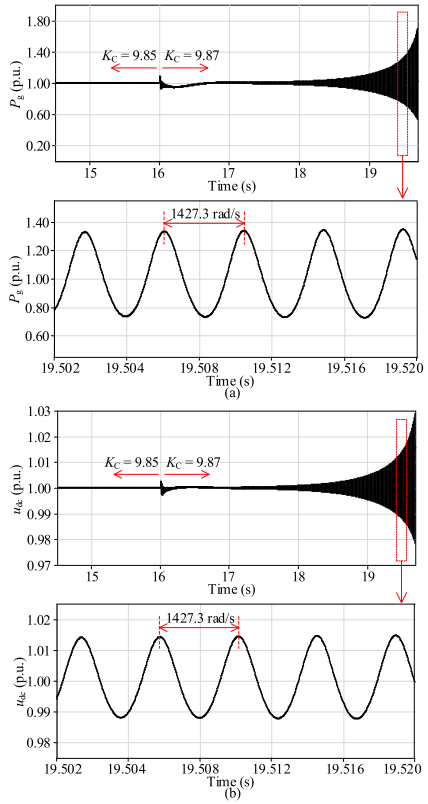

FIGURE 23. Simulation results of the ISynC-based wind turbine system with virtual capacitor control and stabilization control when K_C increases from 9.85 to 9.87. (a) Output power of the GSC. (b) Dc-link voltage.

Fig. 23 shows simulation results of the ISynC-based wind turbine system with virtual capacitor control and stabilization control when K_C increases from 9.85 to 9.87, where k_{SCR} is 2, and K_{PSS} is 8. In Fig. 23, when K_C increases at 16 s, the output power of the GSC and the dc-link voltage begin to oscillate and become unstable. The oscillation frequency in Fig. 23 is 1427.3 rad/s, which is close to the analytical oscillation frequency in Table 4. Simulation results in Fig. 23 are consistent with theoretical analysis in Fig. 17, proving that the proposed method can improve the system stability up to an extent.

D. PERFORMANCE OF INERTIAL RESPONSES WITH STABILIZATION CONTROL

Fig. 24 shows the simulation results of the ISynC-based wind turbine system with virtual capacitor control and stabilization control when the grid frequency drops, where K_C is 8, k_{SCR} is 2, K_{PSS} is 8, and the wind speed is 11 m/s. In Fig. 24, when

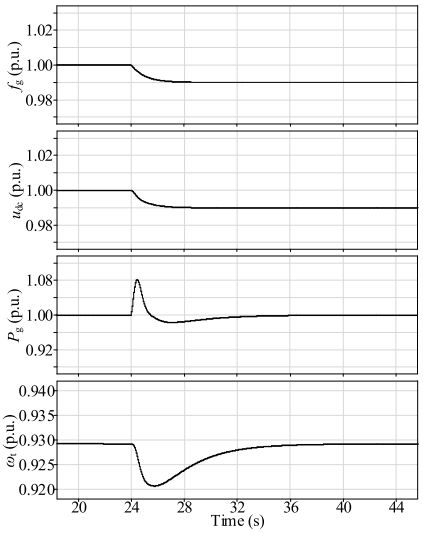

FIGURE 24. Responses of the ISynC-based wind turbine system with virtual capacitor control and stabilization control when the grid frequency drops.

f_g drops from 1.00 p.u. to 0.99 p.u. at 24 s, u_{dc} drops from 1.00 p.u. to 0.99 p.u. accordingly. At the same time, the output power of the GSC increases 0.08 p.u., and recovers later. The wind turbine speed decreases about 0.01 p.u. and recovers later.

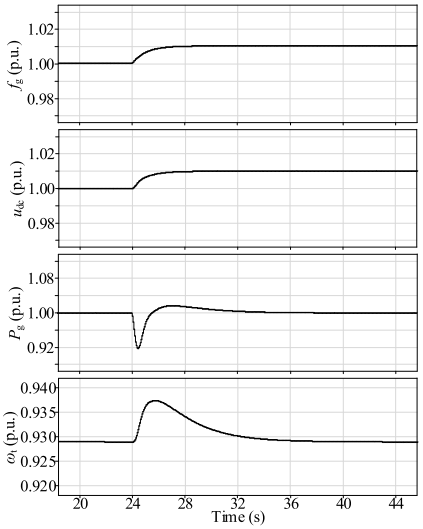

FIGURE 25. Responses of the ISynC-based wind turbine system with virtual capacitor control and stabilization control when the grid frequency rises.

Fig. 25 shows the simulation results of the ISynC-based wind turbine system with virtual capacitor control and stabilization control when the grid frequency rises, where K_C is 8, k_{SCR} is 2, K_{PSS} is 8, and the wind speed is 11 m/s. In Fig. 25, when f_g rises from 1.00 p.u. to 1.01 p.u. at 24 s, u_{dc} rises from 1.00 p.u. to 1.01 p.u. accordingly. At the same time, the output power of the GSC decreases 0.08 p.u., and recovers later. The wind turbine speed increases about 0.01 p.u. and recovers later.

It can be seen from Fig. 24 and Fig. 25 that the active power absorbed and released by the wind turbine during inertial response increases from less than 0.01 p.u. to 0.08 p.u. comparing with Fig. 20 and Fig. 21. Benefiting from the introduction of stabilization control, the virtual capacitor coefficient can be tuned to a large value, which will enhance the inertial response effect and achieve good grid-frequency support.

VII. CONCLUSION

Other than the typical VSG realization which emulates the electromechanical dynamics of a SG, this paper employs and modifies the idea using the capacitor voltage of the converter to fulfill the PLL-less grid-synchronization. To improve the capability of inertial response and the stable operation in weak grids, both the virtual capacitor control and the stabilization control are proposed. Together with the new synchronization technique, a comprehensive control method for the Type-IV wind turbine is achieved.

Efforts of this work are made on analyzing and clarifying the feasibility and stability of such control method, which are crucial both from a practical and a theoretical viewpoint. In this regard, a detailed start-up validation is conducted, and the overall system stability is evaluated through eigenvalue analysis along with mechanism analysis of instability. Several findings of mechanism analysis results based on the ''complex power coefficient method'' are:

1) Increasing the virtual capacitance coefficient will reduce the MSC's damping power coefficient, which leads to instability.

2) The proposed stabilization control method by introducing the feedback of dc-link voltage to the GSC's modulation voltage will increase the GSC's damping power coefficient, thereby improving the system stability.

All the analyses are verified by time domain simulations in PSCAD/EMTDC, proving that the proposed control strategies can provide satisfactory inertial response under weak grid conditions.

In addition, one of the evident benefits of ISynC left for future works is that, the intrinsic ''frequency-lock'' property of the ISynC can be applied to the HVDC systems, where a non-communication-based inertial response can be easily achieved by implementing this property.

APPENDIX

Matrices A, B and C from (40) can be expressed in (61)–(63), as shown at the bottom of this page.

$$A=\begin{bmatrix}
\frac{-I_{gd}U_g}{2H_C} & \frac{-I_{gq}U_g}{2H_C} & 0 & 0 & 0 & 0 & 0 & 0 & \frac{-U_g}{2H_C} & 0\\
\omega_{Bg} & 0 & 0 & 0 & 0 & 0 & 0 & 0 & 0 & 0\\
0 & 0 & \frac{-\omega_{Bm}k_{pc}}{L_s} & 0 & \frac{\omega_{Bm}}{L_s} & 0 & 0 & 0 & 0 & 0\\
0 & 0 & 0 & \frac{-\omega_{Bm}k_{pc}}{L_s} & 0 & \frac{\omega_{Bm}}{L_s} & 0 & 0 & 0 & 0\\
0 & 0 & -k_{ic} & 0 & 0 & 0 & 0 & 0 & 0 & 0\\
0 & 0 & 0 & -k_{ic} & 0 & 0 & 0 & 0 & 0 & 0\\
0 & 0 & 0 & 0 & 0 & 0 & 0 & 0 & 0 & 0\\
\frac{1}{T} & 0 & 0 & 0 & 0 & 0 & 0 & \frac{-1}{T} & 0 & 0\\
k_{SCR}U_g\omega_{Bg} & 0 & 0 & 0 & 0 & 0 & 0 & 0 & -k_{SCR}R_g\omega_{Bg} & \omega_{Bg}\\
0 & k_{SCR}U_g\omega_{Bg} & 0 & 0 & 0 & 0 & 0 & 0 & -\omega_{Bg} & -k_{SCR}R_g\omega_{Bg}
\end{bmatrix} \tag{61}$$

$$B=\begin{bmatrix}
\frac{1}{2H_C} & 0 & 0 & 0 & 0 & 0 & -k_{is} & 0 & 0 & 0\\
0 & 0 & 0 & \frac{\omega_{Bm}k_{pc}}{L_s} & 0 & k_{ic} & 0 & 0 & 0 & 0\\
0 & 0 & 0 & 0 & 0 & 0 & k_{is} & 0 & 0 & 0
\end{bmatrix}^T \tag{62}$$

$$C=\begin{bmatrix}
\frac{k_{ps}k_{pc}K_CI_{sq}}{k_1T} & 0 & \frac{U_{md}-I_{sq}L_s}{k_1} & \frac{U_{mq}+k_{pc}I_{sq}}{k_1} & 0 & \frac{-I_{sq}}{k_1} & \frac{-k_{pc}I_{sq}}{k_1} & \frac{-k_{ps}k_{pc}K_CI_{sq}}{k_1T} & 0 & 0\\
\frac{-\left(k_{ps}^2I_{sq}+k_1\right)k_{pc}K_C}{k_1T} & 0 & \frac{k_{ps}\left(I_{sq}L_s-U_{md}\right)}{k_1} & \frac{-k_{ps}\left(U_{mq}+k_{pc}I_{sq}\right)}{k_1} & 0 & \frac{k_{ps}I_{sq}}{k_1} & \frac{k_1+k_{ps}k_{pc}I_{sq}}{k_1} & \frac{-\left(k_{ps}^2I_{sq}+k_1\right)k_{pc}K_C}{k_1T} & 0 & 0\\
\frac{-K_C}{T} & 0 & 0 & 0 & 0 & 0 & 0 & \frac{K_C}{T} & 0 & 0
\end{bmatrix} \tag{63}$$

REFERENCES

[1] J. Tan and Y. Zhang, "Coordinated control strategy of a battery energy storage system to support a wind power plant providing multi-timescale frequency ancillary services," *IEEE Trans. Sustain. Energy*, vol. 8, no. 3, pp. 1140–1153, Jul. 2017.
[2] L. Harnefors, X. Wang, A. G. Yepes, and F. Blaabjerg, "Passivity-based stability assessment of grid-connected VSCs—An overview," *IEEE J. Emerg. Sel. Topics Power Electron.*, vol. 4, no. 1, pp. 116–125, Mar. 2016.
[3] J. Quintero, V. Vittal, G. T. Heydt, and H. Zhang, "The impact of increased penetration of converter control-based generators on power system modes of oscillation," *IEEE Trans. Power Syst.*, vol. 29, no. 5, pp. 2248–2256, Sep. 2014.
[4] Y. Sun, H. Ye, X. Sun, and F. Miao, "Wind power fluctuation mitigation based low-frequency oscillation," *J. Eng.*, vol. 2017, no. 13, pp. 1299–1306, 2017.
[5] Y. Xu and Y. Cao, "Sub-synchronous oscillation in PMSGs based wind farms caused by amplification effect of GSC controller and PLL to harmonics," *IET Renew. Power Gener.*, vol. 12, no. 7, pp. 844–850, May 2018.
[6] C. Zhang, X. Cai, Z. Li, A. Rygg, and M. Molinas, "Properties and physical interpretation of the dynamic interactions between voltage source converters and grid: Electrical oscillation and its stability control," *IET Power Electron.*, vol. 10, no. 8, pp. 894–902, Jun. 2017.
[7] J. H. R. Enslin and P. J. M. Heskes, "Harmonic interaction between a large number of distributed power inverters and the distribution network," *IEEE Trans. Power Electron.*, vol. 19, no. 6, pp. 1586–1593, Nov. 2004.
[8] A. Rygg, M. Molinas, C. Zhang, and X. Cai, "On the equivalence and impact on stability of impedance modeling of power electronic converters in different domains," *IEEE J. Emerg. Sel. Topics Power Electron.*, vol. 5, no. 4, pp. 1444–1454, Dec. 2017.
[9] W. Du, X. Chen, and H. Wang, "PLL-induced modal resonance of grid-connected PMSGs with the power system electromechanical oscillation modes," *IEEE Trans. Sustain. Energy*, vol. 8, no. 4, pp. 1581–1591, Oct. 2017.
[10] D. Gautam, L. Goel, R. Ayyanar, V. Vittal, and T. Harbour, "Control strategy to mitigate the impact of reduced inertia due to doubly fed induction generators on large power systems," *IEEE Trans. Power Syst.*, vol. 26, no. 1, pp. 214–224, Feb. 2011.
[11] A. Mullane and M. O'Malley, "The inertial response of induction-machine-based wind turbines," *IEEE Trans. Power Syst.*, vol. 20, no. 3, pp. 1496–1503, Aug. 2005.
[12] A. Saffarian and M. Sanaye-Pasand, "Enhancement of power system stability using adaptive combinational load shedding methods," *IEEE Trans. Power Syst.*, vol. 26, no. 3, pp. 1010–1020, Aug. 2011.
[13] J. Morren, S. W. H. de Haan, W. L. Kling, and J. A. Ferreira, "Wind turbines emulating inertia and supporting primary frequency control," *IEEE Trans. Power Syst.*, vol. 21, no. 1, pp. 433–434, Feb. 2006.
[14] J. M. Mauricio, A. Marano, A. Gómez-Expósito, and J. L. M. Ramos, "Frequency regulation contribution through variable-speed wind energy conversion systems," *IEEE Trans. Power Syst.*, vol. 24, no. 1, pp. 173–180, Feb. 2009.
[15] Y. Wang, J. Meng, X. Zhang, and L. Xu, "Control of PMSG-based wind turbines for system inertial response and power oscillation damping," *IEEE Trans. Sustain. Energy*, vol. 6, no. 2, pp. 565–574, Apr. 2015.
[16] H. T. Ma and B. H. Chowdhury, "Working towards frequency regulation with wind plants: Combined control approaches," *IET Renew. Power Gener.*, vol. 4, no. 4, pp. 308–316, Jul. 2010.
[17] J. Brisebois and N. Aubut, "Wind farm inertia emulation to fulfill Hydro-Québec's specific need," in *Proc. IEEE Power Energy Soc. Gen. Meeting*, San Diego, CA, USA, Jul. 2011, pp. 1–7.
[18] C. Zhang, X. Cai, A. Rygg, and M. Molinas, "Sequence domain SISO equivalent models of a grid-tied voltage source converter system for small-signal stability analysis," *IEEE Trans. Energy Convers.*, vol. 33, no. 2, pp. 741–749, Jun. 2018.
[19] D. Dong, J. Li, D. Boroyevich, P. Mattavelli, I. Cvetkovic, and Y. Xue, "Frequency behavior and its stability of grid-interface converter in distributed generation systems," in *Proc. IEEE 27th Annu. Appl. Power Electron. Conf. Expo. (APEC)*, Orlando, FL, USA, Feb. 2012, pp. 1887–1893.
[20] X. Chen, Y. Zhang, S. Wang, J. Chen, and C. Gong, "Impedance-phased dynamic control method for grid-connected inverters in a weak grid," *IEEE Trans. Power Electron.*, vol. 32, no. 1, pp. 274–283, Jan. 2017.
[21] A. Rygg, M. Molinas, C. Zhang, and X. Cai, "A modified sequence-domain impedance definition and its equivalence to the dq-domain impedance definition for the stability analysis of AC power electronic systems," *IEEE J. Emerg. Sel. Topics Power Electron.*, vol. 4, no. 4, pp. 1383–1396, Dec. 2016.
[22] B. Wen, D. Boroyevich, R. Burgos, Z. Shen, and P. Mattavelli, "Impedance-based analysis of active frequency drift islanding detection for grid-tied inverter system," *IEEE Trans. Ind. Appl.*, vol. 52, no. 1, pp. 332–341, Jan./Feb. 2016.
[23] D. Dong, B. Wen, D. Boroyevich, P. Mattavelli, and Y. Xue, "Analysis of phase-locked loop low-frequency stability in three-phase grid-connected power converters considering impedance interactions," *IEEE Trans. Ind. Electron.*, vol. 62, no. 1, pp. 310–321, Jan. 2015.
[24] S. Sang, N. Gao, X. Cai, and R. Li, "A novel power-voltage control strategy for the grid-tied inverter to raise the rated power injection level in a weak grid," *IEEE J. Emerg. Sel. Topics Power Electron.*, vol. 6, no. 1, pp. 219–232, Mar. 2018.
[25] J. Driesen and K. Visscher, "Virtual synchronous generators," in *Proc. IEEE Power Energy Soc. Gen. Meeting Convers. Del. Elect. Energy 21st Century*, Pittsburgh, PA, USA, Jul. 2008, pp. 1–3.
[26] Q.-C. Zhong and G. Weiss, "Synchronverters: Inverters that mimic synchronous generators," *IEEE Trans. Ind. Electron.*, vol. 58, no. 4, pp. 1259–1267, Apr. 2011.
[27] P.-L. Nguyen, Q.-C. Zhong, F. Blaabjerg, and J. M. Guerrero, "Synchronverter-based operation of STATCOM to mimic synchronous condensers," in *Proc. 7th IEEE Conf. Ind. Electron. Appl. (ICIEA)*, Singapore, Jul. 2012, pp. 942–947.
[28] L. Zhang, L. Harnefors, and H.-P. Nee, "Power-synchronization control of grid-connected voltage-source converters," *IEEE Trans. Power Syst.*, vol. 25, no. 2, pp. 809–820, May 2010.
[29] L. Zhang, L. Harnefors, and H.-P. Nee, "Interconnection of two very weak AC systems by VSC-HVDC links using power-synchronization control," *IEEE Trans. Power Syst.*, vol. 26, no. 1, pp. 344–355, Feb. 2011.
[30] F. Milano, F. Dörfler, G. Hug, D. J. Hill, and G. Verbič, "Foundations and challenges of low-inertia systems," in *Proc. Power Syst. Comput. Conf. (PSCC)*, Dublin, Ireland, Jun. 2018, pp. 1–25.
[31] J. He, K. Wu, L. Huang, H. Xin, C. Lu, and H. Wang, "A coordinated control scheme to realize frequency support of PMSG-based wind turbines in weak grids," in *Proc. IEEE Power Energy Soc. Gen. Meeting (PESGM)*, Portland, OR, USA, Aug. 2018, pp. 1–5.
[32] T. Jouini, C. Arghir, and F. Dörfler, "Grid-friendly matching of synchronous machines by tapping into the DC storage," in *Proc. 6th IFAC Workshop Distrib. Estimation Control Netw. Syst.*, Tokyo, Japan, 2016, pp. 192–197.
[33] I. Cvetkovic, D. Boroyevich, R. Burgos, C. Li, M. Jaksic, and P. Mattavelli, "Modeling of a virtual synchronous machine-based grid-interface converter for renewable energy systems integration," in *Proc. IEEE 15th Workshop Control Modeling Power Electron. (COMPEL)*, Santander, Spain, Jun. 2014, pp. 1–7.
[34] A. Etxegarai, P. Eguia, E. Torres, and E. Fernandez, "Impact of wind power in isolated power systems," in *Proc. 16th IEEE Medit. Electrotech. Conf.*, Yasmine Hammamet, Tunisia, Mar. 2012, pp. 63–66.

SHUN SANG (S'19) was born in Jiangsu, China, in 1991. He received the B.S. degree in electrical engineering from the China University of Mining and Technology, Jiangsu, in 2014. He is currently pursuing the Ph.D. degree with the Wind Power Research Center, Shanghai Jiao Tong University, Shanghai, China.

He was a Ph.D. Visiting Scholar with the Department of Engineering Cybernetics, Norwegian University of Science and Technology, Trondheim, Norway, in 2018. His current research interests include the control of wind turbines, interactive stability issues between wind power converters and AC grids.

CHEN ZHANG received the B.Eng. degree in electrical engineering from the China University of Mining and Technology, Xuzhou, China, in 2011, and the Ph.D. degree from Shanghai Jiao Tong University, Shanghai, China, in 2018.

Since 2018, he has been with the Department of Engineering Cybernetics, Norwegian University of Science and Technology, Trondheim, Norway, where he is currently a Postdoctoral Researcher. His current research interests include modeling and stability analysis of VSC-based energy conversion systems, where the aim is to reveal the fundamental dynamics and stability mechanisms of renewable energies with VSCs as the grid interface.

XU CAI received the B.Eng. degree from Southeast University, Nanjing, China, in 1983, and the M.Sc. and Ph.D. degrees from the China University of Mining and Technology, Jiangsu, China, in 1988 and 2000, respectively.

He was with the Department of Electrical Engineering, China University of Mining and Technology, as an Associate Professor, from 1989 to 2001. In 2002, he joined Shanghai Jiao Tong University, as a Professor, where he has been the Director of the Wind Power Research Center, since 2008 and also the Vice Director of the State Energy Smart Grid R&D Center, Shanghai, from 2010 to 2013. His research interests include power electronics and renewable energy exploitation and utilization, including wind power converters, wind turbine control systems, large power battery storage systems, clustering of wind farms and its control systems, and grid integration.

MARTA MOLINAS (M'94) received the Diploma degree in electromechanical engineering from the National University of Asuncion, Asuncion, Paraguay, in 1992, the M.E. degree from Ryukyu University, Nishihara, Japan, in 1997, and the Ph.D. degree from the Tokyo Institute of Technology, Tokyo, Japan, in 2000.

She was a Guest Researcher with the University of Padova, Padova, Italy, in 1998. From 2004 to 2007, she was a Postdoctoral Researcher with the Norwegian University of Science and Technology (NTNU), where she was a Professor with the Department of Electric Power Engineering, from 2008 to 2014. She is currently a Professor with the Department of Engineering Cybernetics, NTNU. Her research interests include stability of power electronics systems, harmonics, instantaneous frequency, and nonstationary signals from the human and the machine.

She has been an AdCom Member of the IEEE Power Electronics Society, from 2009 to 2011. She is an Associate Editor of the IEEE JOURNAL OF EMERGING AND SELECTED TOPIC IN POWER ELECTRONICS, the IEEE TRANSACTIONS ON POWER ELECTRONICS and an Editor of the IEEE TRANSACTIONS ON ENERGY CONVERSION.

JIANWEN ZHANG (M'15) received the B.S., M.S., and Ph.D. degrees from Shanghai Jiao Tong University, China, in 2003, 2006, and 2014, respectively, all in electrical engineering. Since 2006, he has been a Faculty Member with Shanghai Jiao Tong University. He has been a Postdoctoral Research Fellow with the School of Mechatronic Systems Engineering, Simon Fraser University, Canada, since 2016.

His current research interests include topologies, control strategies and reliability issue of high-power renewable energy conversion systems, integration of renewable energy and distributed generation, flexible HVDC power transmission, and DC distribution systems.

FANGQUAN RAO received the Degree in electrical engineering from the Harbin Institute of Technology, Harbin, China, in 1958.

From 1958 to 1966, he was an Electrical Engineer with Harbin Electrical Machinery Works. From 1966 to 1999, he was with the Dongfang Electrical Machinery Company Ltd., Deyang, China, where he was the Chief Engineer and also the Deputy Director, from 1983 to 1999. He took part in a number of significant hydropower projects of China, such as designing generators for power station Longyangxia (320 MW), and organized research on the 300-MW turbo generator and the hydro-generator with evaporation cooling system, which received the Second Prize of the Chinese National Science and Technology Promotion. In 1999, he joined Shanghai Jiao Tong University, Shanghai, China, where he is currently a Professor with the Electrical Engineering Department. His research interest includes the control of large electrical generators, special electrical machines.

Prof. Rao became a Member of the Chinese Academy of Engineering, in 1995. He received the First Prize of the Chinese National Science and Technology Promotion from the Chinese Government and the Outstanding Prize of the Science and Technology Promotion of Sichuan Province.